Cross laminated timber at in-plane shear loading

Strength and Fracture analysis of shear mode III

Danielsson, Henrik; Serrano, Erik

Published in:
World Conference on Timber Engineering (WCTE 2021)

2021

Document Version:
Publisher's PDF, also known as Version of record

WCTE 2021
WORLD CONFERENCE ON TIMBER ENGINEERING
SANTIAGO, CHILE | 9 - 12 AUGUST

CROSS LAMINATED TIMBER AT IN-PLANE SHEAR LOADING – STRENTH AND FRACTURE ANALYSIS OF SHEAR MODE III

Henrik Danielsson[1], Erik Serrano[2]

ABSTRACT: Theoretical investigations of Cross Laminated Timber (CLT) at in-plane shear loading conditions are presented with focus on shear failure mode III, relating to shear stresses acting in the crossing areas between orthogonally bonded laminations of different layers. Failure criteria for structural design, test configurations and material parameters are discussed. Full 3D finite element (FE) analyses applying a cohesive zone approach were used to study the load-bearing capacity and the fracture behaviour at in-plane shear loading. Stress distributions found from FE-analysis are presented and the behaviour at mixed mode loading situations, involving uniaxial shear loading and torsional loading, is discussed.

KEYWORDS: CLT, in-plane shear, failure mode III, finite element modelling, fracture mechanics

1 INTRODUCTION

For design of Cross Laminated Timber (CLT) at in-plane shear loading conditions as illustrated in Figure 1, three different failure modes are generally considered: gross shear failure (FM I), net shear failure (FM II) and shear failure in the crossing areas (FM III). Shear FM III is relevant for elements without edge-bonding and relates to the shear stresses acting in the flatwise bonded area between orthogonally oriented laminations placed in adjacent layers in the element thickness direction.

The paper deals with theoretical investigations based on fracture mechanics considering CLT at in-plane shear loading conditions with focus on shear FM III.

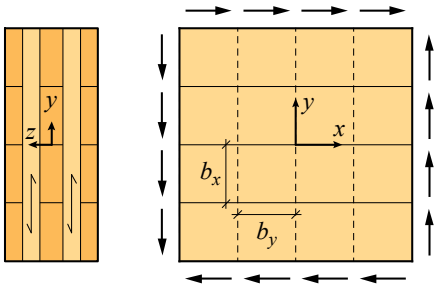

Figure 1: *Cross laminated timber at in-plane shear loading*

[1] Henrik Danielsson, Division of Structural Mechanics, Lund University, P.O. Box 118, SE-221 00 Lund, Sweden. Email: henrik.danielsson@construction.lth.se
[2] Erik Serrano, Division of Structural Mechanics, Lund University, Sweden.

1.1 FAILURE CRITERIA FOR SHEAR FM III

At in-plane shear loading of CLT, by *pure shear loading* or by shear loading from *in-plane beam loading* conditions, relative translation and rotation between two orthogonally bonded laminations give rise to shear stresses in the crossing area connecting the laminations. These stresses act in the *xy*-plane as defined in Figure 1 and relate to shear FM III.

For design regarding shear FM III, the following failure criteria based on linear interaction between stress components have been proposed in e.g. [1] and [2]

$$\frac{\tau_{tor}}{f_{v,tor}}+\frac{\tau_{zx}}{f_{v,R}} \le 1.0 \quad \text{and} \quad \frac{\tau_{tor}}{f_{v,tor}}+\frac{\tau_{zy}}{f_{v,R}} \le 1.0 \qquad (1a, 1b)$$

where τ_{tor} is the shear stress due to the torsional moment M_{tor} and where τ_{zx} and τ_{zy} are the shear stresses due to shear forces F_x and F_y, respectively, as illustrated in Figure 2.

The shear stress τ_{tor} is assumed to be equal to the maximum shear stress at the midpoints of the edges of the crossing area, as calculated from linear elastic theory using the polar moment of inertia of the bonded area

$$\tau_{tor}=\frac{M_{tor}}{I_{P,CA}}\frac{b_{max}}{2} \qquad \text{where} \quad I_{P,CA}=\frac{b_x b_y}{12}\left(b_x^2+b_y^2\right) \qquad (2)$$

where b_x and b_y are the widths of the laminations oriented in the *x*- and *y*-directions, respectively (see Figure 1), and where $b_{max} = \max\{b_x, b_y\}$. The strength parameter, $f_{v,tor}$, refers to the corresponding nominal stress calculated from the maximum torsional loading in a test.

The shear stress components τ_{zx} and τ_{zy} are in design commonly assumed to be uniformly distributed over the crossing area and the corresponding strength value, $f_{v,R}$, refers to the rolling shear strength of the laminations.

From the view of continuum mechanics, it is confusing that the stress components – τ_{tor}, τ_{zx} and τ_{zy} – are evaluated against two different strength values: the rolling shear strength $f_{v,R}$ for stress components τ_{zx} and τ_{zy} and a torsional shear strength $f_{v,tor}$ for the torsional shear stress τ_{tor}. In this sense, the torsional shear strength should be viewed as a structural property, rather than a material property.

The considered shear stress components τ_{zx} and τ_{zy} acting in the crossing area represent, for the *longitudinal* lamination shown in Figure 2, longitudinal shear and rolling shear, respectively. For the *orthogonally* bonded lamination of the same crossing area, τ_{zx} and τ_{zy} represent instead rolling shear and longitudinal shear, respectively.

An alternative approach for verification of load-bearing capacity is outlined in [3]. The main idea of that approach is to consider *only* the rolling shear strength and to consider no interaction of the shear stress components, due to the large difference between rolling shear and longitudinal shear strength values, $f_{v,R}$ and f_v, respectively. Instead of using Equations (1a) and (1b), the following failure criterion is suggested to be investigated

$$\max\left\{\frac{\tau_{zx}}{f_{v,R}}, \frac{\tau_{zy}}{f_{v,R}}\right\} \leq 1.0 \qquad (3)$$

where τ_{zx} and τ_{zy} are the shear stresses acting in the crossing area due to *any* combination of uniaxial shear forces F_x and F_y and torsional moment M_{tor}.

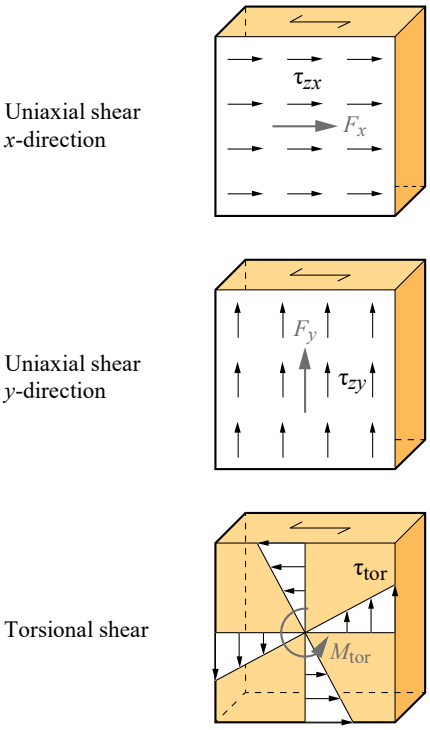

Figure 2: *Shear stress components τ_{zx}, τ_{zy} and τ_{tor}*

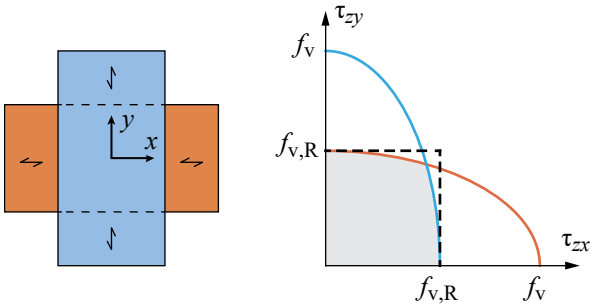

Figure 3: *Suggested failure criterion based on only rolling shear strength $f_{v,R}$ (dashed lines)*

Failure criteria for *each* of the two lamination surfaces of a crossing area, based on quadratic interaction between longitudinal shear and rolling shear and assuming $f_v = 2f_{v,R}$, are illustrated by red and blue curves in Figure 3. The dashed lines represent the suggested criterion according to Equation (3).

The approach outlined in [3] and the failure criterion given in Equation (3) would make it possible to abandon the torsional shear strength parameter $f_{v,tor}$, and instead use only the rolling shear strength $f_{v,R}$ as the determining material property parameter.

1.2 AIM AND OBJECTIVES

The aim of the work presented in this paper is to investigate the possibilities of adopting failure criteria for shear FM III which are based on a rational treatment of the involved stress components. Making use of the failure criterion (3), only the rolling shear strength, which has a clear physical interpretation, is needed, without the need to introduce a parameter such as $f_{v,tor.}$ Non-linear finite element (FE) analyses were performed to investigate the load-bearing capacity and fracture course for shear FM III in CLT at different loading situations, considering mixed uniaxial shear force loading and torsional loading.

A test configuration for a single CLT-node, used to determine the strength parameters $f_{v,R}$ and $f_{v,tor}$, has been analysed using full 3D FE-models. The bonding between the laminations was modelled using a cohesive zone approach, including strain softening behaviour after reaching the local material strength.

Specific objectives of the numerical studies were to investigate; (a) whether the assumed shear stress distributions shown in Figure 2 agree with stress distributions found from FE-analyses and (b) investigate the feasibility of using failure criteria based on Equation (3).

2 TESTS OF SINGLE NODES

Experimental tests of single crossing areas exposed to uniaxial shear and pure torsion are for example presented in [4, 5].

The results presented in [5] are based on the test setup illustrated in Figure 4, which allows for loading in either pure uniaxial shear, pure torsion, or a combination of both modes of loading.

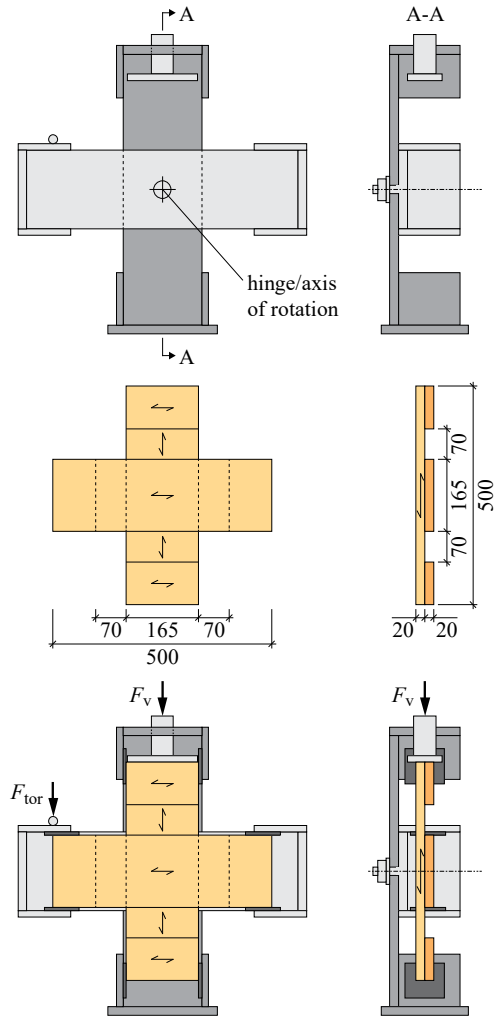

Figure 4: *Test setup and specimen for testing of single CLT-nodes with loading in uniaxial shear, torsion, or mixed mode of loading. Modified after [5]*

For loading in pure uniaxial shear (F_v in Figure 4) and evaluation of the average shear stress in the crossing area at maximum applied load, a mean rolling shear strength $f_{v,R} = 1.26$ MPa was found. For the case of pure torsional loading (F_{tor} in Figure 4), a torsional shear strength $f_{v,tor} = 2.97$ MPa was found by evaluation of the maximum applied torsional moment according to Equation (2).

Combined states of loading were also tested. For these tests, the specimens were first loaded in uniaxial shear up to either about 35% or about 50% of the mean value of the maximum loads found from the tests in pure uniaxial shear. Keeping the uniaxial shear loading constant, torsional loading was applied until failure. Results obtained for the mixed mode load-bearing capacities of these tests agree with the linear interaction according to Equations (1a) and (1b).

Test results for pure torsional loading are also reported in [4], using a test setup very similar to the setup shown in Figure 4. A total of 34 tests were carried out on specimens made from Norway spruce, using a melamine-based adhesive for 24 specimens and a one-component polyurethane adhesive for 10 specimens. The mean density of the laminations was 423 kg/m^3 and the moisture content was 10±1%. The mean torsional shear strength, evaluated according to Equation (2), was found to be $f_{v,tor} = 2.80$ MPa for the specimens bonded with the melamine-based adhesive and $f_{v,tor} = 3.43$ MPa for the specimens bonded with the one-component polyurethane adhesive.

3 ANALYTICAL MODELS

Approaches for estimation of the load-bearing capacity at shear mode III loading of CLT can be formulated based on simple analytical models. The models presented here are based on the stress state within a shear compliant medium of infinitesimal thickness, which is placed between to two rigid surfaces. Loading of the crossing area can be applied by uniaxial relative translation or relative rotation of the two rigid surfaces.

Two possible *limit stress* surfaces (or *yield* surfaces), surface A and surface B, for the in-plane shear stresses τ_{zx} and τ_{zy} are illustrated in Figure 5. A limit shear stress f_s for uniaxial shear loading is considered for both surfaces A and B. Stress interaction is considered for surface A, while no interaction between the two shear stress components is considered for surface B.

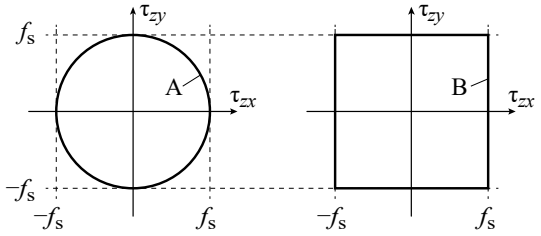

Figure 5: *Yield surfaces A and B*

Thus, the failure criteria can be expressed as:

$$\text{Surface A:} \qquad \sqrt{\tau_{zx}^2 + \tau_{zy}^2} \le f_s \tag{4}$$

$$\text{Surface B:} \qquad \max\{\tau_{zx}, \tau_{zy}\} \le f_s \tag{5}$$

Load-bearing capacities for pure uniaxial shear loading in either direction (F_x or F_y) and pure torsional loading (M_{tor}) are given below, for the case of a square crossing area with side lengths $b_x = b_y = b$. Indices A and B refer to yield surfaces A and B, respectively, and indices E and P refer to the elastic and plastic capacities, respectively. Plastic capacities are based on assuming a perfectly plastic behaviour after reaching the limit/yield stress f_s and adopting an associated flow rule.

The load-bearing capacity (elastic and plastic) for uniaxial shear in either direction is obviously the same for both loading directions and both yield surfaces, and given by

$$F_{x/y,E,A} = F_{x/y,E,B} = F_{x/y,P,A} = F_{x/y,P,B} = b^2 f_s \tag{6}$$

Pure torsional loading and use of yield surface A results in an elastic load-bearing capacity according to

$$M_{tor,E,A} = \frac{I_{P,CA}}{b/\sqrt{2}} f_s = \frac{\sqrt{2}}{6} b^3 f_s \approx 0.2357\, b^3 f_s \tag{7}$$

corresponding to the limit stress being reached simultaneously at the four corner points of the glued surface of the crossing area.

Pure torsional loading and use of yield surface B results in an elastic load-bearing capacity according to

$$M_{\text{tor,E,B}} = \frac{I_{\text{P,CA}}}{b/2} f_{\text{s}} = \frac{1}{3} b^3 f_{\text{s}} \approx 0.3333\ b^3 f_{\text{s}} \tag{8}$$

corresponding to the limit stress being reached simultaneously along the four edges of the glued surface of the crossing area.

The ultimate plastic capacities for pure torsional loading are finally given by

$$M_{\text{tor,P,A}} = f_{\text{s}} \int_A \sqrt{x^2+y^2}\, \mathrm{d}A \approx 0.3826\ b^3 f_{\text{s}} \tag{9}$$

$$M_{\text{tor,P,B}} = \frac{4}{9} b^3 f_{\text{s}} \approx 0.4444\ b^3 f_{\text{s}} \tag{10}$$

Predicted load-bearing capacities according to these analytical models are used for comparison to the results of the numerical model presented below.

4 NUMERICAL MODEL

Non-linear finite element (FE) analyses have been performed using the software Abaqus [6, 7]. The test configuration shown in Figure 4 was studied and the response at loading was analysed using a full 3D FE-model, considering small displacement analyses. A cohesive zone approach including strain softening was used to model the fracture behaviour within the crossing area.

The laminations were modelled as 3D solids, considering linear elastic and orthotropic material behaviour. Rectilinear material principal directions were used with the longitudinal (L) direction oriented in the length direction of the laminations, the tangential (T) direction oriented in the lamination width direction and the radial (R) direction oriented in the lamination thickness direction. Stiffness parameters used for the laminations in the numerical analyses are given in Table 1.

Linear 8-node elements with full integration (denoted C3D8 in Abaqus) were used. Three different FE-mesh densities were applied for the laminations, with elements of close to cubic shape. The three mesh densities had element side lengths of approximately 10 mm, 5 mm, or 2 mm corresponding to FE-meshes with 2, 4, or 10 elements in the thickness direction (20 mm) of one lamination.

The face bonding between the two laminations, constituting the tested crossing area, was modelled using a cohesive zone approach including strain softening behaviour after reaching the local material strength. This behaviour was modelled using a surface-to-surface contact formulation. Hard contact was considered for compression over the crossing area. For the two in-plane shear directions and for tension, an initial linear elastic contact stiffness was applied with equal stiffness values in all three directions and uncoupled behaviour. This stiffness can be thought of as representing the small compliance of the bond line itself, in the elastic state. The stiffness parameters were in most analyses set as $k_{\text{n}} = k_{\text{s1}} = k_{\text{s2}} = 100$ N/mm^3. The influence of the stiffness parameters on the predicted load-bearing capacity was also studied, since their value influence the stress distribution and influence the stability of the solution; too stiff values may lead to ill-conditioned systems of equations. In previous investigations, see e.g. [8, 9], stiffness values of 100–1000 N/mm^3 provided a good balance between reasonable representation of the stiffness of the bond line, without resulting in ill-conditioned systems of equations.

A stress-based criterion for damage initiation was adopted according to the following maximum stress criterion

$$\max\left\{\frac{\langle\sigma_{\text{n}}\rangle}{f_{\text{n}}}, \frac{\tau_{\text{s1}}}{f_{\text{s1}}}, \frac{\tau_{\text{s2}}}{f_{\text{s2}}}\right\} = 1.0 \tag{11}$$

where σ_{n} is the normal (tensile) stress and where τ_{s1} and τ_{s2} are the two in-plane shear stresses. The strength values f_{n}, f_{s1} and f_{s2} represent the local material strengths, i.e. the maximum stress before damage and stiffness degradation is initiated. For the current application and orientation of material principal directions, f_{n} corresponds to the perpendicular to grain tensile strength (in the R-direction). The two shear strengths f_{s1} and f_{s2} correspond to either longitudinal or rolling shear in the two bonded laminations. Adopting the maximum stress criterion given in Equation (11) and using equal in-plane shear strength values gives a damage initiation criterion corresponding to the criterion given in Equation (3) and illustrated in Figure 3. The material strength parameters (maximum stresses) adopted for the analyses presented here are: $f_{\text{n}} = 5$ MPa and $f_{\text{s1}} = f_{\text{s2}} = 3$ MPa. The shear strengths in the two in-plane directions were for all analyses set equal and the notation $f_{\text{s}} = f_{\text{s1}} = f_{\text{s2}}$ is used below.

Strain softening was modelled using a damage evolution expressed in terms of the fracture energy G_{f} and resulting in a linear response between the contact stresses and the relative displacements (contact surface shear slips and normal separation). The value of the fracture energy was for most analyses assumed as $G_{\text{f}} = 1200$ Nm/m^2, except for the parameter study presented below where the influence of the fracture energy on the predicted load-bearing capacity was investigated.

Only the specimen itself, i.e. the timber laminations, was modelled and the test arrangement, i.e. the steel parts used for fixation of the specimen and for load introduction, was not modelled. Boundary conditions were imposed by introducing prescribed displacements according to Figure 6.

Table 1: *Material stiffness parameters for laminations*

Modulus of Elasticity	E_{L}	12 000	MPa
	E_{T}	400	MPa
	E_{R}	600	MPa
Shear modulus	G_{LT}	750	MPa
	G_{LR}	600	MPa
	G_{TR}	75	MPa
Poisson's ratio	ν_{LT}	0.50	-
	ν_{LR}	0.50	-
	ν_{TR}	0.33	-

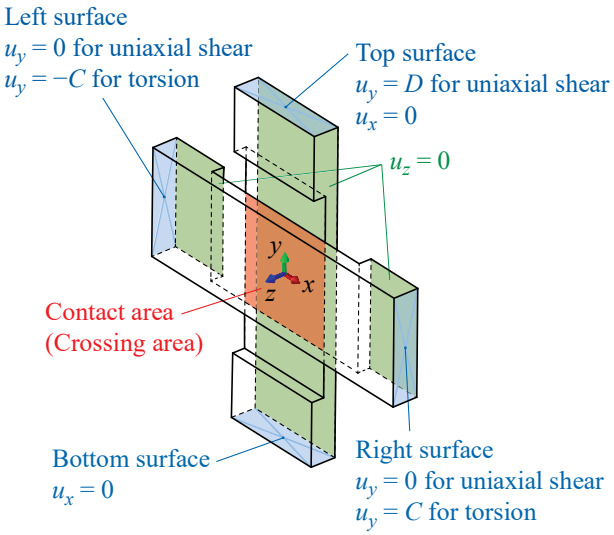

Figure 6: *Boundary conditions for finite element model*

The surfaces marked in blue – denoted *top*, *bottom*, *left* and *right* surface – were constrained by kinematic couplings to the respective midpoint nodes, which were used as reference points. All nodes on the respective surfaces were coupled to the corresponding reference point, such that the surface behaved as a rigid cross section with displacement/rotation according to the reference point. The displacement boundary conditions were in the FE-model applied to the reference points (the midpoints) of the considered surfaces.

5 RESULTS

5.1 INFLUENCE OF FE-MODEL PARAMETERS

The influence on the global response of some FE-model parameters was studied for both pure uniaxial shear force loading and for pure torsional loading. For these analyses, the fracture energy was set to $G_f = 1200$ Nm/m^2, while the contact stiffnesses and the FE-mesh densities were varied.

For contact stiffnesses $k_n = k_{s1} = k_{s2} = 100$ N/mm^3, the differences in maximum loads – compared to the case of 2 mm element side length – were below 1% for an element side length of 10 mm and below 0.1% for an element side length of 5 mm. For the FE-mesh density with an element side length of 5 mm, three values of the elastic contact stiffnesses were used: 100 N/mm^3, 300 N/mm^3 and 600 N/mm^3. The differences in maximum load were for these stiffnesses below 0.1% for pure shear force loading and below 0.3% for pure torsional loading. The results in terms of load-bearing capacity were hence found to be influenced only to a very small extent by varying the contact stiffnesses and the FE-mesh densities within the considered intervals.

5.2 LOAD-DISPLACEMENT RESPONSE AND STRESS DISTRIBUTIONS

Results presented in this section are based on an FE-mesh with element side length of approximately 2 mm, fracture energy $G_f = 1200$ Nm/m^2 and initial contact stiffness parameters $k_n = k_{s1} = k_{s2} = 100$ N/mm^3. The FE-mesh with element side lengths of 2 mm was used for these analyses, to yield a fine spatial resolution of the stress distribution over the crossing area.

Results in terms of the mean shear stress in the y-direction over the crossing areas, τ_{zy}, versus the prescribed displacement are shown in Figure 7 for the case of pure shear force loading. This loading situation was achieved by applying an increasing prescribed displacement $u_y = D$ at the top surface of the specimen, see Figure 6. The mean shear stress was determined from the total shear force F_y and the size of the contact area, $A = b^2$. In Figure 8, the distributions of the shear stress τ_{zy} are shown for a line in the x-direction (from $x = -82.5$ mm to $x = 82.5$ mm) at the centre of the crossing area ($y = 0$ mm) for load stages a)–d), as indicated in Figure 7. The solid line and the marks in Figure 8 represent the stress values found from the FE-analysis, while the dashed lines represent the mean shear stress at the corresponding load.

Point a) in Figure 7 and the curve in Figure 8a correspond to the initiation of damage and softening by creation of a fracture process zone, which takes place at the two top corners of the crossing area ($y = 82.5$ mm, $x = \pm 82.5$ mm). As the loading is increased, the fracture process zones extend and the stress-based damage initiation criterion is met at the midpoints of the vertical edges of the crossing area at loading corresponding to point b) in Figure 7 and the curve in Figure 8b. As the loading is increased further, the fracture process zones extend towards the centre of the crossing area and the load-bearing capacity is finally reached at a mean shear stress of 1.69 MPa, point d) in Figure 7 and Figure 8d.

The shear stress distribution found from the FE-analysis is highly non-uniform over the crossing area, during all stages of the loading. It is also noticeable that the highly non-linear local response is not detectable in the global load versus displacement response shown in Figure 7.

Results in terms of the *apparent* torsional shear stress τ_{tor} versus the prescribed displacement are shown in Figure 9, for the case of pure torsional loading. Pure torsion was applied by prescribing increased displacements at the reference points of the right and left surfaces of the specimen, $u_y = \pm C$, according to Figure 6. The apparent torsional shear stress τ_{tor} was determined according to Equation (2) using the torsional moment M_{tor} as found from the FE-analysis. Similar to the case of pure uniaxial shear loading, the distributions of the shear stress τ_{zy} are shown in Figure 10, for a line along the x-direction at the centre of the crossing area and for load stages a)–d), as indicated in Figure 9. The solid lines and marks represent the shear stress as found from the FE-analysis, while the dashed lines represent the stress magnitude and distribution according to Equation (2).

Damage initiation and softening starts at the four corner points of the crossing area at loading corresponding to point a) in Figure 9. The fracture process zones then extend, along the perimeter of the crossing area and inwards, towards the centre of the crossing area, as the loading is increased. The load-bearing capacity is finally reached at an apparent torsional shear stress of 2.51 MPa, point d) in Figure 9.

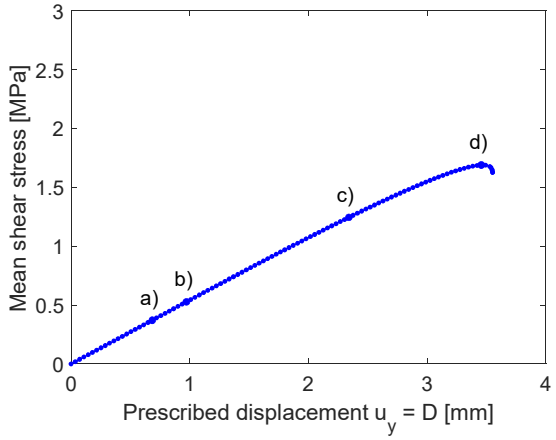

Figure 7: *Mean shear stress τ_{zy} versus prescribed displacement for pure uniaxial shear force loading*

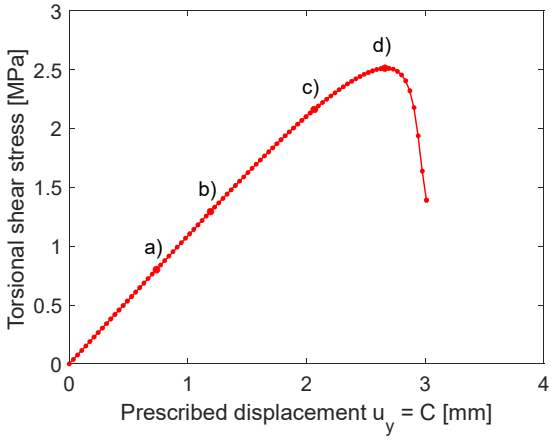

Figure 9: *Torsional shear stress τ_{tor} versus prescribed displacement u_y for pure torsional loading*

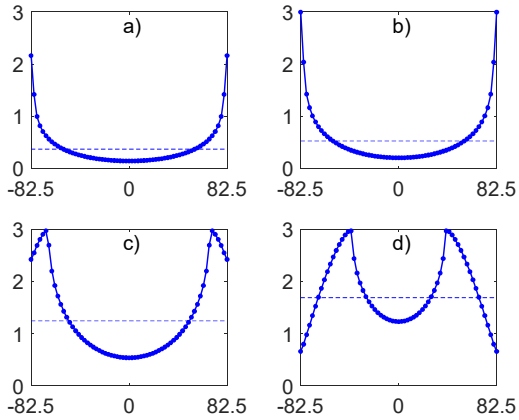

Figure 8: *Distribution of shear stress τ_{zy} across the width of the crossing area (x-direction) for points a)–d) along the load path for pure uniaxial shear force loading according to Figure 7*

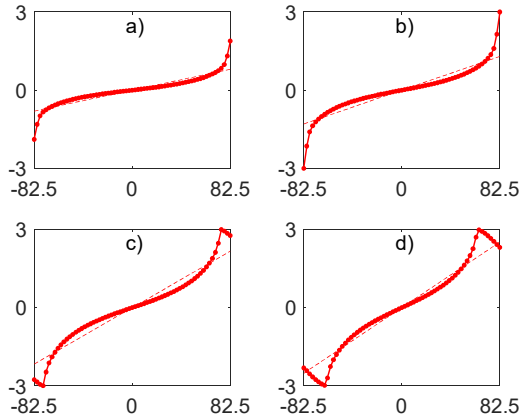

Figure 10: *Distribution of shear stress τ_{zy} across the width of the crossing area (x-direction) for points a)–d) along the load path for pure torsional loading according to Figure 9*

5.3 INFLUENCE OF FRACTURE ENERGY ON LOAD-BEARING CAPACITY

The influence of the fracture energy on the load-bearing capacity at pure uniaxial shear force loading and at pure torsional loading was studied, considering a wide range of values of the fracture energy; G_f = 200–160000 Nm/m^2. Results presented in this section are based on an FE-mesh with element side lengths of approximately 5 mm and contact stiffness parameters $k_n = k_{s1} = k_{s2}$ = 100 N/mm^3.

To facilitate generalisation of the results, a characteristic material length l_{ch} is introduced, see e.g. [10–12]. The characteristic length is determined by material property parameters and defined according to

$$l_{ch} = \frac{G_f G_{TR}}{f_s^2} \tag{12}$$

where G_f is the fracture energy, G_{TR} the rolling shear modulus and f_s the local material shear strength. A brittleness ratio is defined as b/l_{ch}, where b is the side length of the crossing area. With these definitions, the brittleness ratio is a dimensionless number.

Results for pure uniaxial shear force loading are presented in Figure 11, in terms of mean shear stress versus prescribed displacement for different values of the fracture energy G_f. The loading is expressed as the mean shear stress over the crossing area and the displacement u_y refers to the applied prescribed displacement of the top surface of the specimen.

Results in terms of the normalised mean shear stress at maximum load are presented in Figure 12, for different values of brittleness ratio b/l_{ch}. The stress values are here normalised with respect to the local material strength f_s = 3.0 MPa. The dashed line (value 1.0) corresponds to the elastic/plastic load-bearing capacities according to yield surfaces A and B according to Equations (4), (5) and (6). For low values of the brittleness ratio b/l_{ch}, i.e. high values of the fracture energy G_f, the normalised mean shear stress at maximum load approaches 1.0 which corresponds to a uniform shear stress distribution and a stress magnitude $\tau_{zy} = f_s$ = 3.0 MPa.

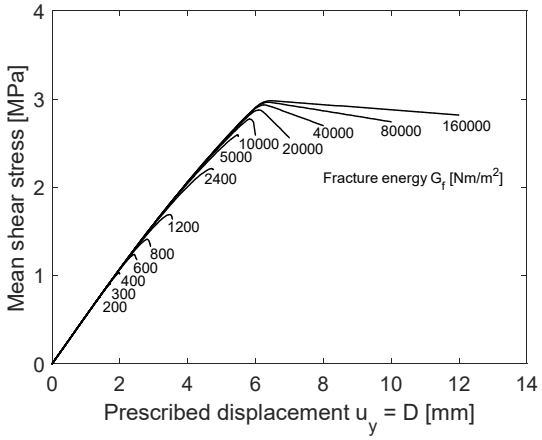

Figure 11: *Mean shear stress versus displacement for different values of the fracture energy G_f (Nm/m^2) for pure uniaxial shear force loading*

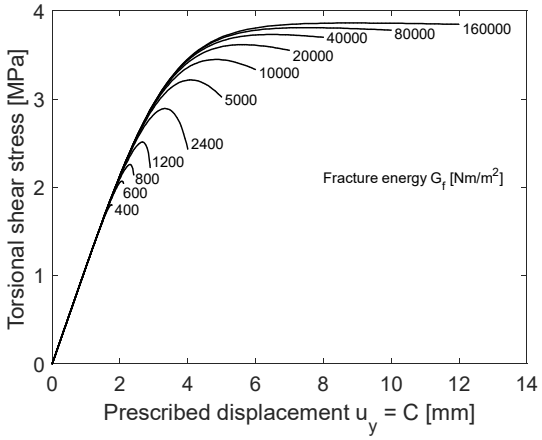

Figure 13: *Torsional shear stress versus displacement for different values of the fracture energy G_f (Nm/m^2) for pure torsional loading*

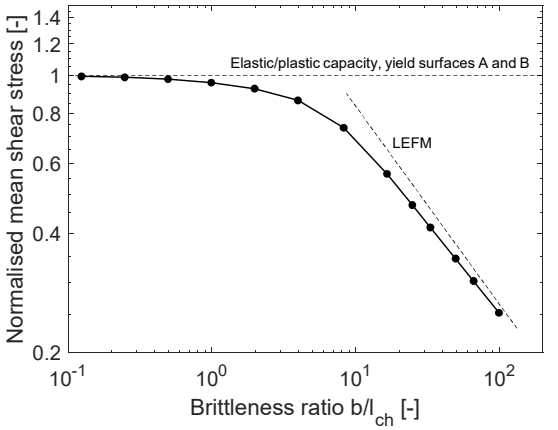

Figure 12: *Normalised mean shear stress at maximum load versus brittleness ration b/l_{ch}, where b = 165 mm*

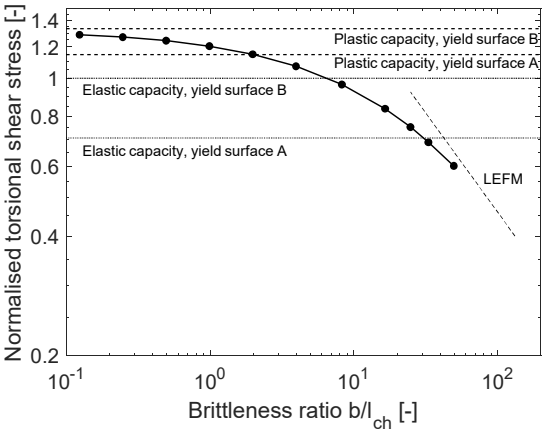

Figure 14: *Normalised torsional stress at maximum load versus brittleness ration b/l_{ch}, where b = 165 mm*

For the case of pure torsional loading, results in terms of load versus displacement are presented in Figure 13, for different values of the fracture energy G_f. The loading is represented by the torsional shear stress as determined from Equation (2) and using the torsional moment M_{tor} as found from the FE-analysis. Results in terms of the normalised torsional shear stress at maximum load are presented in Figure 14, for different values of the brittleness ratio b/l_{ch}. The dotted lines represent the elastic capacities according to limit/yield surfaces A and B while the dashed lines represent the corresponding plastic capacities, see Equations (4–10).

The trends pointed out above for the case of pure uniaxial shear force loading are present also for the case of pure torsional loading. As the brittleness ratio b/l_{ch} decreases, the load-bearing capacity found from the FE-analyses approaches the value given by the plastic load-bearing capacity of limit/yield surface B. In relation to the results presented in Figures 11 to 14, it should be noted that results for fracture energy below 400 Nm/m^2 are not included for the pure torsional loading case. This is due to numerical difficulties encountered at load levels around the expected maximum loads and the brittle global response at low values of the fracture energy.

For high values of the brittleness ratio b/l_{ch}, and assuming all other model parameters being constant, the influence of the fracture energy on the predicted load-bearing capacity appears to correspond to that of Linear Elastic Fracture Mechanics (LEFM). According to LEFM, the nominal strength is proportional to the square root of the fracture energy as indicated by dashed lines in Figures 12 and 14.

5.4 LOAD-BEARING CAPACITY AT MIXED MODE LOADING

Numerical analyses of mixed mode loading situations have also been performed. These analyses were performed using three different types of loading paths for applying the mixed mode load situation using prescribed displacements as illustrated in Figure 6.

Results presented in this section are based on an FE-mesh with element side lengths of approximately 5 mm and contact stiffness parameters $k_n = k_{s1} = k_{s2} = 100$ N/mm^3.

Mixed mode loading – Type #1

A mixed mode of loading according to type #1 was achieved by first applying a pure uniaxial shear loading by increasing prescribed displacement at the top surface.

This loading was applied up to a displacement $u_y = D_{max}$. In a subsequent load step, the displacement at the top surface was kept constant at $u_y = D_{max}$ while torsional loading was applied by increasing displacements $u_y = \pm C$ at the left and right surfaces until reaching the load-bearing capacity. Different states of mixed mode loading were achieved by varying the prescribed maximum displacement of the top surface, $u_y = D_{max}$, before applying the torsional loading.

The loading path according to type #1 is similar to the mixed mode loading procedure described in [5] and reviewed in Section 2: Loading by a pure uniaxial shear force load F_y was first applied up to a certain level and then an increasing torsional loading M_{tor} was applied, while keeping the shear force loading constant.

Mixed mode loading – Type #2

A mixed mode of loading according to type #2 was achieved by applying pure torsional loading in the first load step. The loading was applied by increasing prescribed displacements at the left and right surfaces up to a value of $u_y = \pm C_{max}$. In a subsequent load step, uniaxial shear loading was applied by prescribed displacement of the top surface, $u_y = D$, until reaching the load-bearing capacity and while keeping the displacements of the left and right surfaces at the constant value of $u_y = \pm C_{max}$.

Mixed mode loading – Type #3

Mixed mode loading according to type #3 was achieved by prescribing displacements simultaneously at the top surface (giving uniaxial shear loading) and at the left and right surfaces (giving torsional loading). Different mixed mode loading situations were achieved by varying the ratio between the prescribed displacements at the top surface and at the left and right surfaces, respectively, i.e. the ratio D/C.

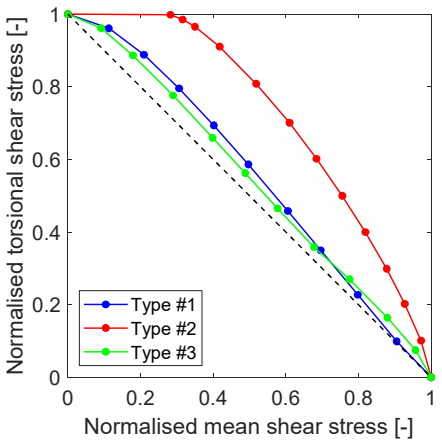

Figure 15: *Normalised torsional shear stress versus normalised mean shear stress at maximum load for mixed mode of loading according to load types #1, #2 and #3*

Results of the load-bearing capacities found from the FE-analyses at mixed mode of loading are presented in Figure 15. The presented stress values refer to the stress at the corresponding maximum load/moment. The *normalised mean shear stress* is determined from the mean shear stress given by the maximum total shear force F_y during loading and the size of the crossing area A, normalised with respect to the value of the corresponding maximum stress at pure uniaxial shear loading, 1.69 MPa. The *normalised torsional shear stress* is determined from the torsional stress according to Equation (2) using the maximum torsional moment M_{tor} during loading. This stress is normalised with respect to the corresponding stress at pure torsional loading, 2.51 MPa.

The FE-analyses gave results which indicate that the mixed mode load-bearing capacity is influenced by the loading path. Applying mixed mode loading according to load types #1 and #3 described above, gave results of the load-bearing capacity similar to the linear interaction between torsion and uniaxial shear as assumed by the design criteria given in Equations (1a) and (1b). A similar response, i.e. a linear interaction, was also found from the tests at mixed mode loading presented in [5], considering mean values of the experimentally found load-bearing capacities using a load application similar to type #1 as described above.

The FE-analyses suggested higher load-bearing capacities for mixed mode loading according to type #2, compared to types #1 and #3. For mixed loading type #2, torsional shear loading is first applied followed by uniaxial shear loading. The differences in predicted load-bearing capacities are related to the development of damage and softening over the crossing area. During the course of the loading, the shear stress distributions over the crossing area change considerably. Some contact points experience loading with increasing contact shear slip in both shear directions while other contact points experience increasing contact shear slip followed by local unloading with decreasing contact shear slip.

In relation to the results presented in Figure 15, it should be noted that these are based on the *maximum* torsional moment and the *maximum* shear force during the complete analysis for a given loading situation. These two maximum values do in general not occur simultaneously. Using loading according to type #1 or type #2, the mixed mode loading condition is imposed by first applying loading by pure shear/rotation and then applying rotation/shear while keeping the previously applied loading constant. With this type of stepwise load application and using loading by prescribed displacements, both the shear force and the torsional moment change during the second load step. Also for loading according to type #3, with simultaneous shear and torsion applied in a single load step, do the two maximum values in general not appear simultaneously.

6 DISCUSSION

For the results presented in Sections 5.2, 5.3 and 5.4, stiffness parameters $k_n = k_{s1} = k_{s2} = 100$ N/mm^3 were used and FE-meshes with element side lengths of either 5 mm or 2 mm were used. These parameters were chosen based on considering the balance between computational time, accuracy in results and numeric stability. For the combination of high values of the brittleness ratio b/l_{ch} and high values of the initial elastic contact stiffness, numerical difficulties were encountered in some analyses and it was then not always possible to reach a clear maximum load. These problems were less pronounced for denser FE-meshes (small elements). To obtain reliable results from the FE-analyses, the size of the fracture process zone typically needs to be sufficiently large in relation to the size of the finite elements.

Typical values for the fracture energy in pure tension perpendicular to the grain for clear wood specimens of softwoods spruce and pine are around 300 Nm/m^2, see e.g. [13] for a compilation of test results. For shear loading of clear wood specimens, giving shear stress and crack propagation along the grain, values of the fracture energy between 680 Nm/m^2 and 1240 Nm/m^2 are for example reported in the literature for spruce and pine, see e.g. [13, 14]. Test data for the fracture energy at shear loading giving rolling shear stress in the direction of crack growth are however scarce. This lack of experimental test data is one motivation for the parameter study of the influence of the fracture energy presented in Section 5.3. The value $G_f = 1200$ Nm/m^2 used for the FE-analyses presented in Sections 5.2 and 5.4, is a rough estimation for the relevant fracture energy for the present application and is based on the corresponding value for longitudinal shear loading. The applied local material shear strength values ($f_{s1} = f_{s2} = 3$ MPa) are also related to uncertainties. The lack of experimental test data motivates further testing to obtain information of relevant material properties.

It should be noted that the highly non-linear response on a local scale, cf. Figures 8a-d, is only to a very limited extent detectable at the global scale of load versus displacement, cf. Figures 7 and 9. As a consequence, it is not possible to draw conclusions on the influence of the non-linear (softening) behaviour of the bond line of the crossing area, based solely on such global response. Consequently, also erroneous conclusions might be drawn about interaction of stress components, failure modes and (lack of) influence of non-linear behaviour such as fracture softening, if evaluations are based only on global force/moment versus displacement/rotation response.

The results regarding mixed mode loading and consideration of the *maximum* shear force and the *maximum* torsional moment found from the FE-analyses during the complete loading phase (Figure 15), are partly difficult to interpret. The loading was applied by prescribed displacements and the two maximum values do then in general not occur simultaneously. The results would probably be partly different for other types of loading scenarios, for example by use of a force-controlled load application.

7 CONCLUDING REMARKS

Numerical studies based on full 3D FE-modelling of CLT-nodes with a single crossing area loaded in pure uniaxial shear, pure torsion and mixed modes of loading have been presented. The long-term and overall aim of the present work is to gain knowledge of the mechanical behaviour and the load-bearing capacity of CLT at in-plane shear loading. This involves exploring the possibilities to use failure criteria based on a rational treatment of the involved stress components and strength properties with a clear physical interpretation.

One important finding from the present study was that the shear stress distributions over the crossing areas found from the FE-analyses differed considerably, compared to the shear stress distributions illustrated in Figure 2 and assumed in practical design situations and used for evaluation of test results. In the linear elastic state, before initiation of damage and softening within the crossing area, highly non-uniform shear stress distributions were for example found from the FE-analyses for the case of pure uniaxial shear force loading (Figure 8a).

The numerical analyses presented here are based on several simplifying assumptions, for example regarding applied boundary conditions, and furthermore related to several uncertainties regarding for example material property parameters. Numerical analyses may however be a useful tool for evaluation of appropriate test setups and loading arrangements, used to determine relevant strength properties needed for structural design of CLT.

Further investigations, including both experimental and theoretical work, is needed in the area. These should include studies of test setups of single crossing areas, as presented here, but also testing of clear wood specimens and bond lines to obtain data for material parameters used as input for numerical analyses.

ACKNOWLEDGEMENTS

The authors would like to acknowledge Prof. Per Johan Gustafsson (1952–2020), who, although no longer with us, made significant contributions to this work.

The financial support from FORMAS for the projects *Cross laminated timber beams – Rational structural analysis* (grant 2016-01090) and *Strength and fracture analysis of cross laminated timber* (grant 2019-01354) is gratefully acknowledged.

The financial support for the project *InnoCrossLam* is also gratefully acknowledged. The project *InnoCrossLam* is supported under the umbrella of ERA-NET Cofund ForestValue by Vinnova, FORMAS and the Swedish Energy Agency. ForestValue has received funding from the European Union's Horizon 2020 research and innovation programme under grant agreement N° 773324.

The computations were enabled by resources provided by the Swedish National Infrastructure for Computing (SNIC) at Lunarc, Lund University, partially funded by the Swedish Research Council through grant agreement no. 2018-05973.

REFERENCES

[1] M. Flaig: Biegeträger aus Brettsperrholz bei Beanspruch in Plattebene. Doctoral thesis. Karlsruhe Institute of Technology, Karlsruhe, Germany, 2013.

[2] M. Flaig, H.J. Blass: Shear strength and shear stiffness of CLT-beams loaded in plane. In: Proc. CIB-W18, CIB-W18/46-12-3, Vancouver, Canada, 2013.

[3] E. Serrano: Test methods for in-plane shear tests of cross laminated timber. In: Properties, testing and design of cross laminated timber: A state-of-the-art report by COST Action FP1402/WG2, Shaker Verlag, Aachen, Germany, 2018.

[4] M. Flaig, N. Meyer: A new test configuration to determine the slip modulus of connections between crosswise bonded boards. In: Experimental Research with Timber, Proceedings of Cost Action FP 1004, Prague, Czech Republic, May 2014.

[5] M. Flaig: Design of CLT Beams with Rectangular Holes or Notches. In: Proc. INTER, INTER/47-12-4, Bath, United Kingdom, 2014.

[6] Dassault Systemes Simulia Corp. ABAQUS/CAE, Version 2019, 2018.

[7] Dassault Systemes Simulia Corp. ABAQUS/CAE, Version 2017, 2016.

[8] H. Danielsson, M. Jeleč, E. Serrano, V. Rajčić: Cross laminated timber at in-plane beam loading – Comparison of model predictions and FE-analyses. Engineering Structures 179:246–254, 2019.

[9] M. Jeleč, H. Danielsson, V. Rajčić, E. Serrano: Experimental and numerical investigations of cross-laminated timber elements at in-plane beam loading conditions. Construction and Building Materials 206:329–346, 2019.

[10] P.J. Gustafsson: Analysis of generalized Volkersen-joints in terms of non-linear fracture mechanics. In: Verchery G, Cardon H, editors. Mechanical behaviour of adhesive joints. Paris, France: Edition Pluralis, p. 323–338, 1987.

[11] E. Serrano. Glued-in Rods for Timber Structures. A 3D Model and Finite Element Parameter Studies. International Journal of Adhesion and Adhesives. 21(2):115–127, 2001.

[12] E. Serrano, P.J. Gustafsson: Fracture mechanics in timber engineering – Strength analyses of components and joints. Materials and Structures 40:87–96, 2006.

[13] H. Danielsson: Perpendicular to grain fracture analysis of wooden structural element – Models and applications. Doctoral thesis. Division of Structural Mechanics, Lund University, 2013.

[14] K. Ostapska: Fracture in wood of Norway spruce – Experimental and numerical study. Doctoral thesis. Department of Structural Engineering, Faculty of Engineering, Norwegian University of Science and Technology, Trondheim, Norway, 2020.